Main Recent Contributions to SHS from France

Jean-Claude Nièpce, Florence Baras, Frédéric A. Bernard, Jean-Pierre Bonnet, Sylvain Dubois, Jean-Claude Gachon, Eric Gaffet, Véronique Gauthier, Annie Lemarchand, Rose-Marie Marin-Ayral, et al.

Main Recent Contributions to SHS from France[1]

J.-C. Nièpce[a, b, c] and GFA members[b, c]

[a] ICB UMR 5209 CNRS-University of Burgundy, Dijon, France
[b] GDR "GFA" 2391 CNRS
[c] PICS 3462 "GFA–ISMAN" CNRS–Russian Foundation for Basic Research (RFBR)
e-mail: jcniepce@u-bourgogne.fr
Members of GFA (French acronym for the French Group of SHS Research),
co-authors of the paper:
Florence Baras (ICB UMR5209, CNRS-UB, Dijon)
Frédéric Bernard (ICB UMR5209, CNRS-UB, Dijon)
Jean-Pierre Bonnet (GEMH, ENSCI, Limoges)
Sylvain Dubois (LMP UMR 6630 CNRS-Univ. Poitiers, CHASSENEUIL-FUTUROSCOPE)
Jean-Claude Gachon (LCSM UMR7555 CNRS-Univ Nancy, Vandoeuvre)
Eric Gaffet (NRG UMR 5060 CNRS-UTBM, Belfort)
Véronique Gauthier (LMP UMR 6630 CNRS-Univ. Poitiers, CHASSENEUIL-FUTUROSCOPE)
Annie Lemarchand (LPTMC UMR 7600 CNRS-Université Pierre et Marie Curie, Paris)
Rose-Marie Marin-Ayral (ICG UMR5253 CNRS-UM2-ENSCM-UM1 PMOF, Montpellier)
Tony Montesin (ICB UMR5209, CNRS-UB, Dijon)
Françoise Nardou (SPCTS UMR6638 CNRS-Unilim-ENSCI, Limoges)
Jean-Claude Nièpce (ICB UMR5209, CNRS-UB, Dijon)
Marie-Christine Record (TECSEN, UMR6122 CNRS-Université Paul Cézanne, Marseille)
Dominique Vrel (LIMHP UPR 1311 CNRS-Paris XIII, Villetaneuse)
Received October 25, 2007

Abstract—Both in situ TRXRD and IR thermography, on the one hand, and different levels of modeling, on the other, have generated a strong progress in the knowledge and control of numerous SHS reactions. The SHS of simple binary materials, such as intermetallics (FeAl, $MoSi_2$, $NbAl_3$, etc.), oxides (e.g. ZrO_2), carbides (e.g. SiC) or nitrides, more complex materials, such as mullite, SiAlONs, MAX phases, composites (SiO_2–Al_2O_3, NiAl–ZrO_2), powders in their more complicated states, such as well controlled microstructures, fully densified intermetallics, smart composites, and hard coatings carried out by GFA researchers greatly contributed to the worldwide competition to harness the potential of SHS. On the occasion of the 40th anniversary of SHS, this paper is giving an overview of the main results obtained by GFA over the last ten years.

Key words: *SHS, MASHS, SPS, SiC, $MoSi_2$, intermetallics, Ti_3SiC_2, SiALONs, composites, coatings, TRXRD*

PACS numbers: 81.05.Je, 81.20.Ka

DOI: 10.3103/S1061386207040115

INTRODUCTION

About ten years ago, the French researchers active in the field of SHS decided to federate themselves in order to build a strong cooperation; as a result, GFA has been created. Then GFA has been supported as a GDR (Group of Research) by French CNRS (National Council for Scientific Research) and, more recently, the cooperation between GFA, in France, and ISMAN, in Russia, has been also supported by a PICS (International Program for Scientific Cooperation) program. The power of collaboration has enriched a lot the French scientific progress in the field: nice in situ TRXRD experiments using the synchrotron radiation coupled with a fast IR camera, experimental and theoretical approaches of the reaction mechanisms, mechanical activation of SHS reactions, production of new interesting materials and of fully dense nano-intermetallics. The paper is giving an overview of the main results. Although the distinction between basic research and applied research is not often well defined, these results are presented with a main reference to the basic interest or to a possible application.

---

[1] Presented at the *International Conference on Historical Aspects of SHS in Different Countries*, October 22–27, 2007, Chernogolovka, Moscow, Russia.

Table 1. Technical improvements of in situ TRXRD experiments implemented by the French SHS group

Systems	Authors	Experiments
NiZr	Bérar et al., *Nucl. Inst. Met. Phys. Res.*, 1993	LURE D43—Detector 17° (2θ) 30 ms × 2000 XRD pattern
Al–Ti–Ni	Javel et al., *J. Alloys Comp.*, 1997	LURE D43—Detector 17° (2θ) 30 ms × 2048 XRD pattern
FeAl	Chariot et al., *Acta Mater.*, 1999	LURE D43—Detector 17 + 30° (2θ) 180 ms × 2048 scans *coupled* with IR thermography
$MoSi_2$	Gras et al., *Acta Mater.*, 1999	LURE D43—Detector 30° (2θ) 50 ms × 2048 scans *coupled* with IR thermography
FeAl, AlTiNi	Bernard et al., *J. Synch. Rad.*, 2000	LURE D43—Detector 17 + 30° (2θ) 33 ms × 2048 scans *coupled* with IR thermography
$NbAl_3$	Gauthier et al., *Intermetallics*, 2002	LURE D43—Detector 30° (2θ) 100 ms × 2048 scans *coupled* with IR thermography
$FeSi$, $FeSi_2$	Gras et al., *Intermetallics*, 2002	LURE D43—Detector 30° (2θ) 50 ms × 2048 scans *coupled* with IR thermography
FeAl	Vrel et al., *Rev. Sci. Instr.*, 2002	LURE H10—Detector INEL 80° (2θ) 30 ms × 2048 scans *coupled* with IR thermography
TiC–NiAl	Curfs et al., *J. Eur. Ceram. Soc.*, 2002	ESRF—High Speed CCD Camera 100 ms, 20° (2θ).
$MoSi_2$	Gras et al., *Intermetallics*, 2006	LURE H10—Detector INEL 80° (2θ) 50 ms × 2048 scans *coupled* with IR thermography
Ti_3SiC_2	Gauthier et al., *J. Am. Ceram. Soc.*, 2006	LURE H10—Detector INEL 80° (2θ) 30 ms × 2048 scans *coupled* with IR thermography
TiN	Carole et al., *J. Alloys Comp.*, 2007	LURE H10—Detector INEL 95° (2θ) 40 ms × 1024 scans *coupled* with IR thermography
Ti(C, N)	Carole et al., *Ceram. Int.*, 2007	LURE H10—Detector INEL 95° (2θ) 40 ms × 1024 scans *coupled* with IR thermography
NiAl, NiAl–ZrO_2	Tingaud et al., *Int. J. SHS*, 2007	LURE H10—Detector INEL 80° (2θ) 30 ms × 2048 scans *coupled* with IR thermography
$MoSi_2$	Cabouro et al., *Acta Mater.*, 2007	ESRF—Detector INEL 120° (2θ) 40 ms × 2048 scans *coupled* with IR thermography

SHS STILL NEEDS BASIC RESEARCH

Experimental Facilities for in situ Monitoring of SHS Reactions

Conventional techniques do not allow the study of the intimate mechanisms which control SHS reactions, such as the role of liquid formation, the existence and effects of transient phases and of other parameters which may induce changes in the microstructure or nature of end products. Real time in situ investigations of structural changes and chemical dynamics in the combustion area have been made possible by the use of synchrotron radiation. Table 1 summarizes the technical improvements which have been implemented by the French SHS group from 1993 to perform time resolved X-ray-diffraction (TRXRD) studies of self-sustained reactions.

For these in situ TRXRD experiments, specific devices have been developed to determine the structural evolution during SHS: a fast detector to monitor the phase transformations and a high-temperature reaction chamber working in vacuum or under low gas pressure. In addition, the thermal evolution during an SHS reaction is determined by means of an IR camera. However, this camera has to record the sample surface temperature, variation rate of which may attain a value up to 1500 deg s^{-1}.

In this paper, the advantages of simultaneous in situ recordings of both the TRXRD patterns, using the high intensity synchrotron radiation, and the sample surface temperature profiles, using a fast IR camera (AVIO TVS 200ST), are shown on some examples.

From 1999 until 2003, TRXRD experiments were performed on H10 in LURE (Orsay, France). These experiments are presently transferred on D2AM-BM2 in ERSF (Grenoble, France) (Fig. 1) while waiting for a beam line (in 2008) in the new French synchrotron SOLEIL (Saclay, France). The schematic sketch of the experimental setup is shown in Fig. 1b [1–3].

A pair of slits is used to minimize the X-ray spot size on the sample in the direction perpendicular to the combustion front. The synchrotron X-ray beam coming from the left corner in Fig. 1b through the entrance slits, hits the sample which is inside a small chamber (Figs. 1, 2a). Air-tightness of the chamber is ensured by
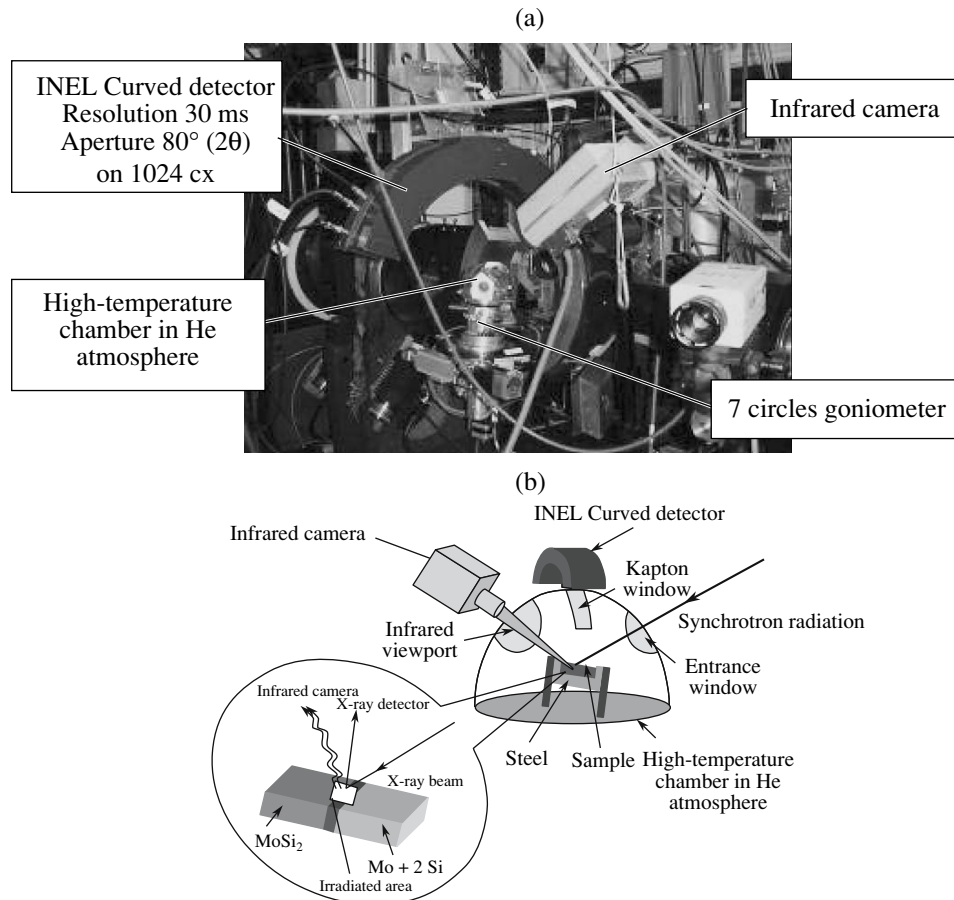
(a)

(b)

Fig. 1. (a) Overall view of the TRXRD device used on the D2AM-BM2 beam line and (b) its schematic sketch [3].

a 190° Kapton window, parallel to the curved detector; Kapton is used in order to have a better wear resistance than Mylar. XRD patterns are recorded by a curved detector (CPS 120 INEL) having a 120° angular aperture which is adjusted versus the expected definition. The acquisition time between two consecutive diffraction patterns is usually ranged between 30 and 100 ms. The high-temperature reaction chamber is located on a 7-circles goniometer featuring 0.001° precision and a vertical adjustment. For IR analysis, a 38 mm diameter calcium fluoride window is used (Fig. 1b). This window has a good transparency from near ultraviolet (UV) to mid infrared (IR) (over 90% transmission from 300 nm to 8 μm). The IR camera is equipped with a lens exhibiting a field of view of 9.5 cm × 6.25 cm and each pixel of one IR picture corresponds to an area of 0.79 × 0.79 mm. The IR thermography is capable of giving a two-dimensional representation of the temperature evolution at the sample surface. The emissivity value, for example for the Mo–Si system before and after reaction, remains within 0.8 and 0.9 and never exhibits large variation between the initial and final steps. Such IR data allow obtaining the propagation wave characteristics, like the combustion front velocity U and the

combustion front stability, especially along two directions (Fig. 2c): (i) along AB, the direction of combustion front propagation and (ii) along CD, which is the perpendicular direction. The positions of IR thermograms recorded along AB during the combustion front passage for three consecutive selected areas (x_1, x_2, x_3) and along CD at the middle of the sample ($x = 0$ mm) are plotted in Fig. 2c.

The experimental setup shown in Fig. 2 has been described in [1, 2]. It is mainly built in aluminum alloy, except for the insulating parts where PTFE is mainly used, and for near-sample or near-igniter parts, stainless steel or even graphite have been selected. The reaction chamber is composed of three parts (Figs. 2a, 2b): (1) top of the chamber, (2) sample holder and (3) goniometer adapter. The sample holder has been designed in order to have a better understanding of phase transitions occurring during a current-activated SHS-sintering (similar to SPS process) (Figs. 2b, 2c). The electric power is supplied by an adjustable high intensity current provided by a 0–250 V, 20 A variable transformer followed by a 220 to 12 V, 200 A regular transformer. The sample holder allowing the passage of an electrical current through the sample has been developed by
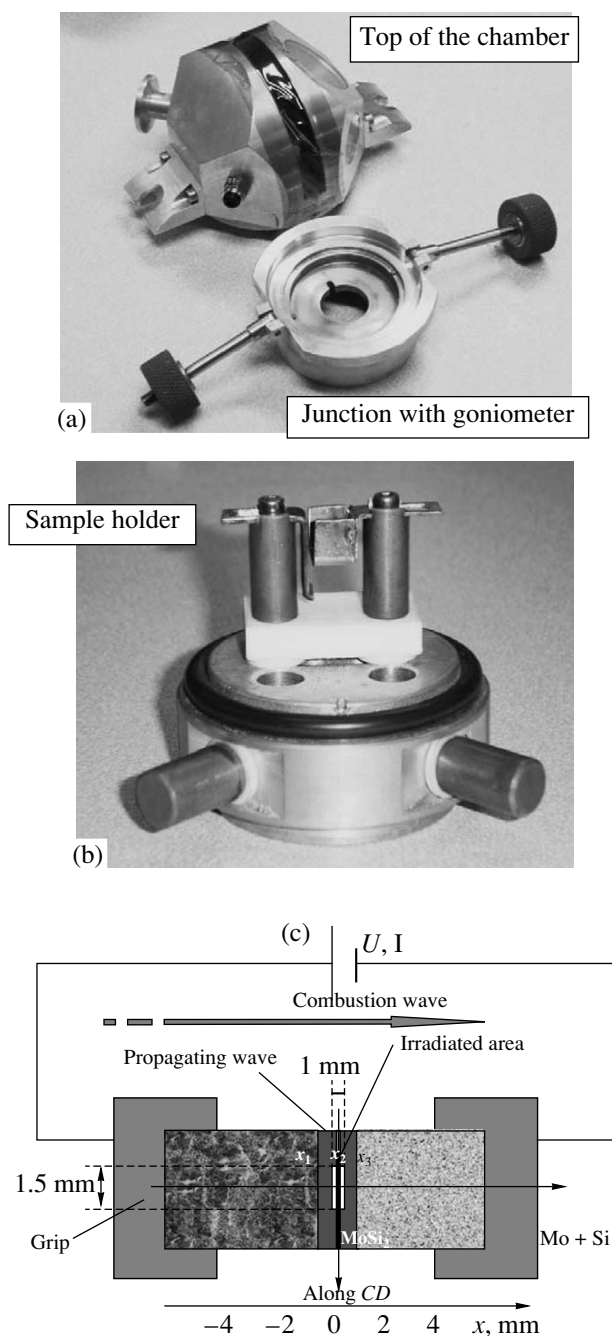
Fig. 2. (a) Reaction chamber, (b) sample holder affording to pass an electric current through the sample, and (c) schematic of SHS experiment, including sample position and positions of IR thermograms recorded during the process along AB (x_1, x_2, x_3) and along CD [3].

S. Paris for the Fe–Al system [2]. It allows fast sample setup, easy adjustments and control of the reaction ignition. Samples are placed between two steel grips. These grips allow heating the powders simultaneously from inside and outside, reproducing the mode of ignition of an SPS device (see below).

INFORMATION ABOUT MECHANISM OF SHS REACTIONS INFERABLE FROM COUPLED IN SITU MEASUREMENTS

SHS of FeAl

A typical experiment might consist of 1024 XRD patterns collected at 30 ms each as shown in Fig. 3b for the Fe + Al ⟶ FeAl reaction. In this figure, the first XRD patterns, recorded just before the reaction ignition, show the distinction between some Al lines and Fe lines. Then the Al [111] and [311] peak intensities, without any superposition with Fe peaks, are reduced to zero corresponding to the aluminum melting. Then, as the combustion wave propagates inside the irradiated area, the FeAl intermetallic phase appears. Simultaneously, a transitory peak corresponding to γ-Fe appears and disappears. Finally, only the FeAl lines are observed.

In this figure, the first XRD patterns recorded just before the reaction ignition show the distinction between some Al lines and Fe lines. Then the Al [111] and [311] peak intensities, without any superposition with Fe peaks, are reduced to zero corresponding to the aluminum melting. Then, as the combustion front wave propagates inside the irradiated area, the intermetallic FeAl phase appears. Simultaneously, a transitory peak which corresponds to γ-Fe appears and disappears. Finally, only the FeAl lines are observed.

SHS of MoSi₂

The experience, TRXRD coupled to IR, and the results were described and discussed in [3]. The IR camera has recorded the thermal evolution at the sample surface during the current-activated SHS sintering starting from mechanically activated (MA) powder mixtures. The reaction time was short. Indeed, after 5.55 s, the combustion front spread through the sample. The analysis of the thermal data performed along the wave propagation axis during the combustion front passage over three consecutive selected areas (x_1, x_2, x_3) (Fig. 2b) showed that the wave propagation was stable. Based on analysis of IR images, the distance between x_1 and x_3 was found to be equal to 3 mm. Measuring the delay between these three thermograms for a fixed temperature (i.e. T_c), the combustion front velocity U could be determined: $U = 15 \pm 1$ mm s^{-1}. The ignition temperature T_{ig} and combustion temperature T_c were found to have a value of 100 and 1440°C, respectively. Similar analysis performed within the irradiated area showed that the wave was not rigorously perpendicular to the axis of the combustion front propagation (Figs. 4c, 4d). The formation of MoSi₂ using the current-activated SHS sintering is very violent; the heating rate v_h being around 3800 deg s^{-1}.

The structural evolution in the irradiated zone during the passage of the combustion front has been investigated using the XRD patterns recorded before, during,
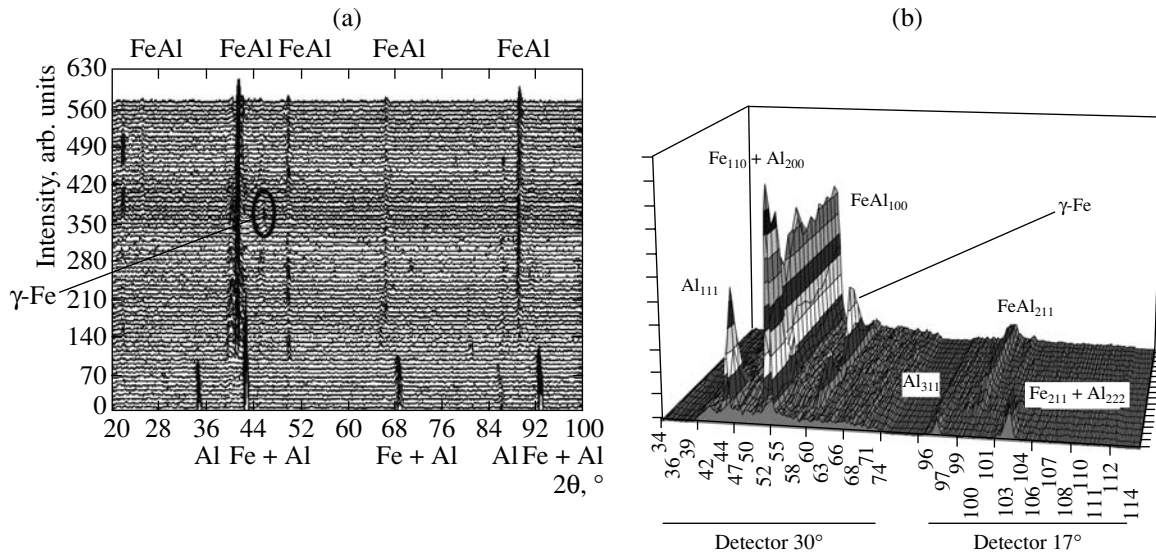
Fig. 3. TRXRD patterns taken during the Fe + Al $\longrightarrow$ FeAl reaction using (a) our second equipment (80° as angular domain, time resolution 30 ms) and (b) our first equipment (30° + 17° as angular domains, a hole of 26° is needed, time resolution 30 ms) [4].

and after the ignition of SHS reaction. Before the combustion front passage, the presence of a negligible quantity of $MoSi_2$ (ICDD 41-0612) which formed during ball milling was highlighted. In the temperature range 500–1000°C, the presence of an intermediate phase, Mo_5Si_3, was detected. Then, the intensity of $MoSi_2$ XRD peak increased. Close to the Si melting temperature, XRD peaks of Mo, Mo_5Si_3 and $MoSi_2$ phases were observed, the volume fraction of Mo_5Si_3 decreased while that of $MoSi_2$, increased. After the combustion front passage, the TRXRD experiment configuration allowed three minutes of sample cooling to be studied. After the SHS reaction, no new phase formation was detected. During cooling down, the volume fractions of Mo_5Si_3 and Mo decreased slightly whereas the volume fraction of $MoSi_2$ increased. Consequently, a mechanism of SHS in the Mo + 2Si system was suggested [3].

SHS of a MAX Compound, Ti_3SiC_2

MAX are ternary compounds, carbides or nitrides, with a lamellar hexagonal crystalline structure and a general formula $M_{n+1}AX_n$, where $n = 1, 2, 3$, M is a transition metal, A = Al, Si, P, S, Ga, Ge, As, and X = C or N. In our case, powders of Ti, Si, and graphite were ball-milled together for 1 h in a Turbula® and then cold pressed into $6 \times 6 \times 4$ mm bars. Green densities were around 55% of the theoretical density. Combustion was performed in a chamber filled with He at ambient pressure to prevent oxidation and/or nitridation of Ti and Si. Samples were held horizontally in a small bench-vice; heat was applied to one end by a strip of graphite foil heated by a DC current source. Coupling TRXRD, IR thermography and post-reaction characterizations, a

tentative mechanism for Ti_3SiC_2 formation has been proposed [5].

During the first step, the TiC_x formation proceeds and the temperature rapidly reaches 2600 K after ignition. Thermodynamically, the Ti + C $\longrightarrow$ TiC_x reaction has indeed the highest reactivity among all possible reactions in the mixture. As this reaction is highly exothermic, it provides local temperature increases, with heating rates around 1000 deg s^{-1}, that are the real ignition sources. Such a first step of the reaction between reactants in Ti–Si–C mixtures is in very good agreement with different previous observations by other authors [6–8]. During heating the 3Ti + Si + 2C powder blend, TRXRD analyses do not indicate any other solid-state reaction; neither Ti_5Si_3 nor $Ti_5Si_3C_x$ intermediate phases were detected. $Ti_5Si_3C_x$ seems to be always formed as an intermediate phase when SiC is used as a silicon source [9, 10].

Thus, the intermediate phases and reaction pathways very likely depend on the type of reactant. It has also been shown previously that the dynamics of phase formation is different in the case of SHS performed with Si or SiC as silicon source [8]. During cooling down to 2000 K, TiC_x is the only phase detected by TRXRD. Although there is no direct formal evidence for the presence of a liquid phase in our TRXRD results, small quantities of liquid phases may likely be present at such a high temperature and heating rates. Indeed, mass balance considerations indicate that TiC_x cannot be the only phase present because it does not contain silicon (from EDS data). Moreover, TiSi, Ti_5Si_3 phases and metastable Tirich–Si solid solution have been observed and identified by coupled XRD, SEM, and EDX analyses. The presence of these phases may result from the solidification of the Ti–Si eutectics at
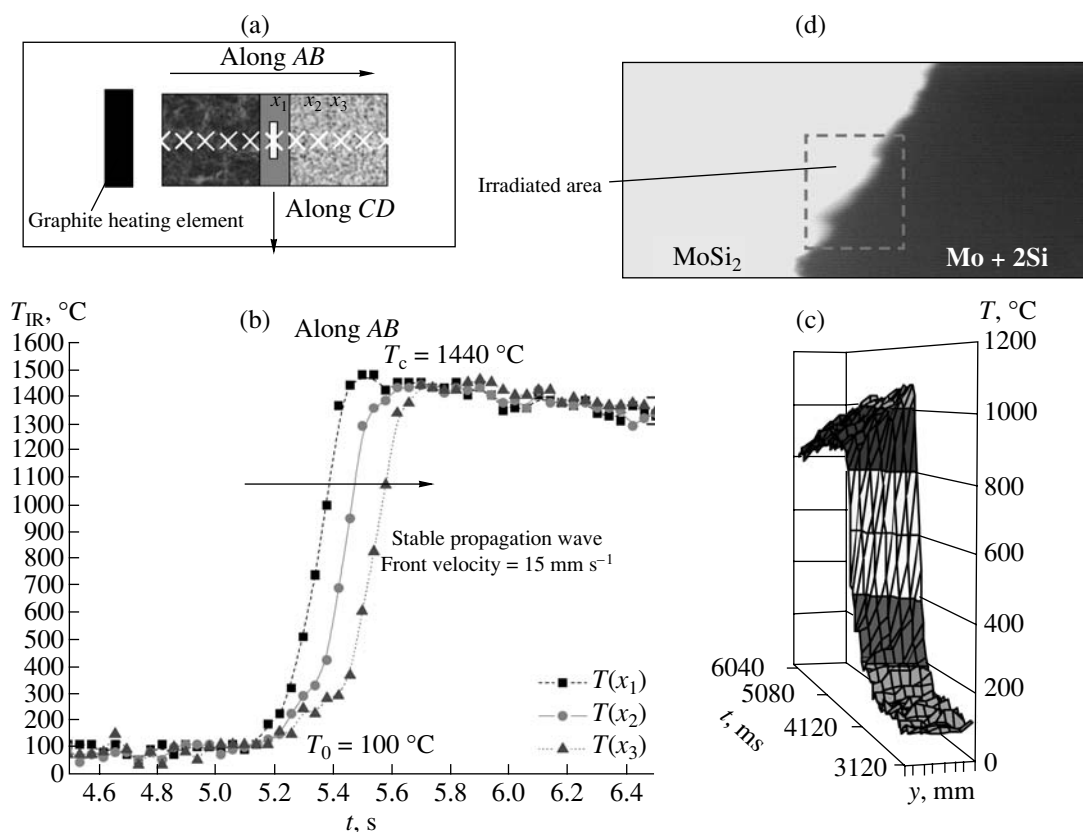
Fig. 4. Thermal analysis of combustion in a Mo + 2Si sample: (a) schematic representation of the sample, (b) combustion front propagation along *AB*, (c) combustion front propagation along *CD*, and (d) macroscopic micrograph of the propagating wave [3].

1830 K and 1580 K which are clearly identified on thermal profiles [5]. Finally, such a Ti–Si liquid phase is also supported by other workers [7, 11]. Thus, TiC_x solid particles are assumed to coexist with a Ti–Si liquid at high temperature. As the Ti_3SiC_2 amount increases and the TiC_x content decreases while the Ti–Si liquid phase is present, nucleation of the MAX phase is heterogeneous in its nature and not homogeneous as discussed in [12, 13]. Such a heterogeneous nucleation is moreover supported by the results of Huang and Chen which show that Ti_3SiC_2 is likely formed from the solid TiC_x and Ti–Si liquid phase [7]. Finally, the Ti–Si liquid phase and solid TiC_x reorganize into the final product of Ti_3SiC_2. Such a formation mechanism is similar to those proposed by Huang and Chen [7] and by Zhang et al. [11]. By decreasing the fluctuation rate, Zhang et al. have indeed shown that the TiC_x amount decreases, which implies that the very stable TiC_x decomposes in the presence of the Ti–Si liquid phase. More work is needed in order to have a better understanding of the interaction between solid TiC_x and Ti–Si liquid phase. An idea may result from the fact that Si can induce twinning of TiC_x and formation of Ti_3SiC_2 platelets [14].

MECHANICAL ACTIVATION OF SHS REACTIONS: MASHS

High-energy ball milling of powder mixtures was reported to be an efficient technique for the preparation of nanocrystalline materials. The mechanical alloying, a basically dry and high-energy milling process, is appropriate for the synthesis of all kinds of materials from metallic to ionic compounds, including materials with non-equilibrium structures. Besides direct synthesis of materials, high energy ball-milling is a way of modifying the conditions in which chemical reactions usually take place either by changing the reactivity of as-milled or by inducing chemical reactions during milling [15]. Mechanical alloying is a complex process which depends on many factors, for instance on physical and chemical parameters such as the energy and frequency of shocks, the duration of milling, the type of mill, ball-to-powder weight ratio, etc. In fact, the ball milling conditions have to be selected for preparing micrometric grains with diffusion couples having different sizes ranging from a few micrometers down to a few nanometers. This step is called mechanical activation (MA) [16]. Then, the combination of MA and SHS was proposed for the synthesis of nanostructured FeAl intermetallics [17]. Now, the Mechanically Activated Self-Propagating High-Temperature Synthesis
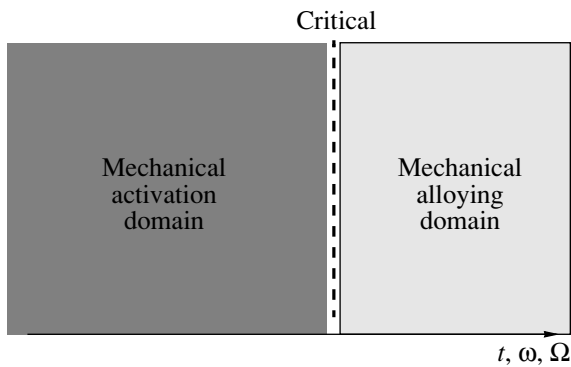
Critical

Mechanical activation domain | Mechanical alloying domain

t, ω, Ω

Fig. 5. Schematic representation of the mechanically activated state vs. ball milling conditions: time t, frequency ω, and energy of shocks Ω [22].

(MASHS) process has been developed for the synthesis of many materials (FeAl [18], NbAl$_3$ [19], MoSi$_2$ [20]).

Description of the Mechanical Activation [21]

The milled particles are trapped between colliding balls or between ball and vial and are subjected to a severe plastic deformation, which exceeds their mechanical strength, accompanied by a temperature rise. During collisions, powders are subjected to high stresses (from 200 MPa up to 2 GPa) for times of the order of microseconds. The delay time between such efficient trapping events is typically of the order of 10 to 100 seconds (depending on the type of milling machine). However, characteristics of the MA end products depend mainly on the nature (ductile or brittle) of the mixture components. Consequently, from the scheme in Fig. 5, the milling duration (before the critical time), all parameters being fixed, has to be selected sufficiently short to avoid the formation of mechanically-induced product phases, but still sufficiently long to form mechanically activated mixtures.

From many authors, the ductile–ductile system is the ideal combination of materials [15, 21] because a true alloying occurs, due to the repeated action of cold welding and fracturing of powder particles. Fracture and welding are the two basic events which produce a permanent exchange of matter between particles and ensure mixing of various elements of ground powders. A layered structure of A and B is thus formed and progressively refined and convoluted. Five typical stages of the evolution of ductile powder mixtures are shown in Fig. 6. Nevertheless, whatever the nature of the mixture components, the milling process which causes an intimate mixing of particles on the nanoscale level leads to both the reduction in the crystallite size and the accumulation of defects in powder particles. All this introduces an additional energy to the reactant system, which effectively lowers the activation barriers for reactions.

We may note that the control of MA agglomerates is essential since they are SHS nanoreactors. Indeed, as an example, Fig. 7 shows that the morphology of Fe/Al agglomerates before and after the reaction are identical.

Effect of MA on SHS Process Parameters

The following significant effects have been evidenced.

(a) Decrease in the ignition temperature (Fig. 8 and Table 2).

(b) Increase in the combustion front velocity U and heating rate v_h (Table 2). In SHS, normal reaction rates are considered to be of the order of 10 mm s^{-1} while propagation rates of the order of 40 mm s^{-1} were measured for some MA alloyed powders. For example, in the Mo–2Si system [20, 23, 26], MA can multiply the U value by a factor of three (up to 42 mm s^{-1}) compared to the classical value obtained under similar ignition conditions. In the same way, the maximum heating rate measured during the combustion process increases, up to $v_h = 6800$ deg s^{-1}, when mechanically activated pow-
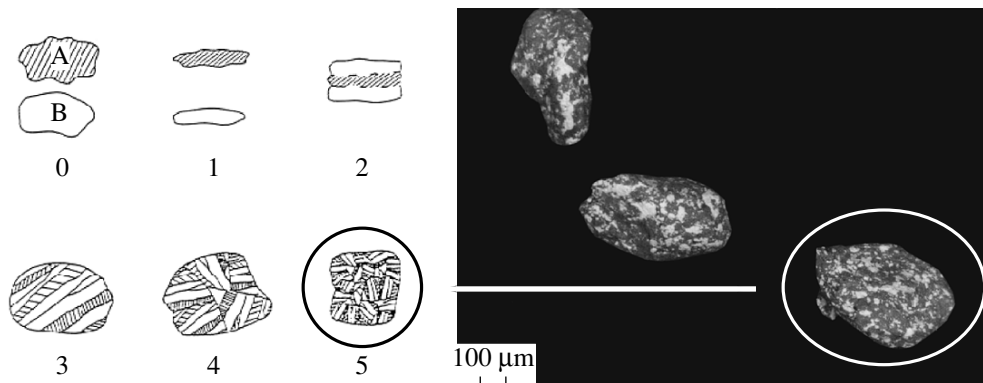

Fig. 6. Stages of powder evolution during ball milling of A (white) and B (hatched) with progressive convolution of lamellae and combination of A with B [16].
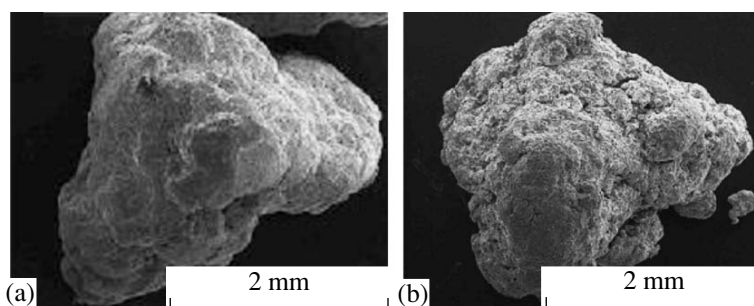
Fig. 7. SEM images of (a) Fe/Al agglomerate before SHS reaction and (b) identical FeAl intermetallic agglomerate after SHS.

ders are used as raw materials. The enhancing influence of MA time on the SHS propagation rate was fairly linear (for 200 rpm alloying) up to 5 h of milling. However, after 6 h, the propagation rate starts to decrease rapidly and powders milled for 7 h or more at 200 rpm do not ignite at all.

(c) In some cases, MA may overcome self-propagation difficulties. Still using the examples of SHS silicides, the SHS process has been successfully applied to a large range of disilicides such as $MoSi_2$, $TaSi_2$, $TiSi_2$, $NbSi_2$ [27–29]. However, only a few papers report an attempt to initiate a combustion reaction in a mixture of elemental reactants (Fe + 2Si) [30]. Indeed, the SHS method is submitted to conditions whereby the heat produced by the reaction should exceed the level needed to initiate the reaction in the next unreacted layer. According to the empirical criterion [31], an exothermic reaction would not become self-sustaining unless $T_{ad} > 1800$ K, where T_{ad} is the maximum temperature reached in the combustion front in adiabatic conditions. Despite an exothermic formation reaction ($\Delta H_{FeSi_2} = -81$ kj mol^{-1}), the production of $FeSi_2$ by direct SHS (Fe + 2Si $\longrightarrow$ $FeSi_2$) is not a favorable case

($T_{ad} = 1300$ K). However, previous work carried out on the Fe–Si system [32, 33] have demonstrated the contrary: proper MA conditions can overcome the thermodynamic obstacle and allow the ignition of a combustion front in cold pressed Fe + 2Si pellets (Fig. 9). Direct activation for the unfavorable Cu–Si system [34] was also reported by Bernard et al. Based on previous in situ analysis [33], it has been clearly established that the Fe/Si combustion wave is directly linked to the formation of FeSi via a solid-state process. In the propagation mode where only a local intense ignition source is used to initiate the process, the combustion front is weak and the reaction is not complete despite the high level of mechanical activation [32, 35]. However, as predicted by an empirical criterion, no combustion wave was observed in case of a simple Turbula mix or a low injected power and short milling duration.

In addition, the SHS experiments with mechanical alloyed Ni–Si powders revealed that MA is essential for allowing SHS processing at room temperature [36]. The unalloyed or 1 h to 2 h milled powders did not react when being heated with a high-temperature glow wire. On the contrary, mixed powders ignited very easily and the propagation rate was higher as compared to conventional SHS after several hours of milling.
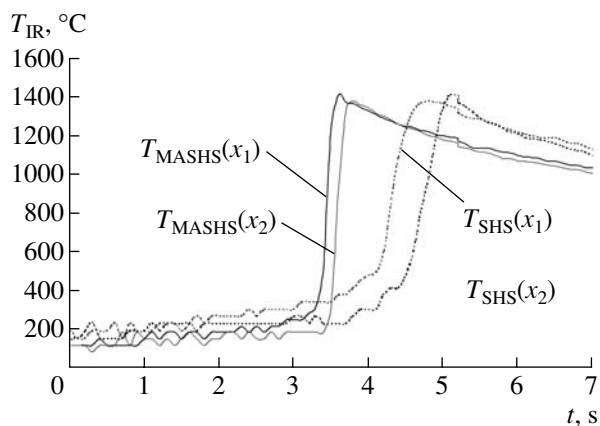
Effect of MASHS on the Microstructure of End Products

Mechanical activation would promote the number of the potential nucleation sites and produce finer crystallites. This conclusion is based on simulations describing the reaction Nb(l) + C(s) $\longrightarrow$ NbC(s) [37] in which it has been reported that a large number of potential germs could decrease the grain size and accelerate the combustion wave. Indeed, still using the Mo–2Si system, it has been shown that high-energy ball milling treatment allows the control of the formation of pure and nanometric α-$MoSi_2$ (88 nm) by fixing the microstructure of reactant powder. In addition, the presence of mechanically alloyed $MoSi_2$ has been found to exhibit a positive effect on the final microstructure because some fractions of mechanically induced $MoSi_2$ act as a heterogeneous nucleation site with a good dis-

Fig. 8. Temperature profiles for classical SHS and for MASHS of $MoSi_2$ [20, 23].

tribution inside the grains and decreases the combustion temperature [38]. Consequently, crystallite growth is limited by the lower temperature, and a large number of grains is formed at the same time.

THERMAL DIFFUSION MEASUREMENTS

Thermal diffusivity seems to play a key role in the propagation of the reaction front; however, for real conditions of the SHS reactions, they are often unknown. So, the aim of this research was to determine transient, high-temperature thermal diffusivity of (freshly) synthesized materials which are difficult to measure by classical methods.

Experiments have been performed with titanium carbide TiC synthesized from the elements. The most significant results have been obtained under a nitrogen atmosphere, for which TiN may be synthesized locally. However, the method can also be applied to the most of SHS systems.

Powders of Ti and C were mixed thoroughly (Turbula mixer, 24 h) and then pressed to a relative density of 60%. Reaction was then ignited in our reaction chamber [1]. When the reaction front reached the end of the sample—because heat transfer occurs faster *within the material* than *between the material and its surrounding*—a hot spot is frequently observed there. When TiC is synthesized under nitrogen, this hot spot can be sufficient to favor the formation of TiN, whose formation enthalpy is even greater than that for TiC. Therefore, the magnitude of this hot spot can be enhanced. In the most intense cases, hot spots 400 to 500 K above the temperature at which the reaction propagates inside the sample have been recorded. Because the end of the sample is then considerably hotter than the rest of the sample, the heat accumulated there can diffuse backwards; therefore, heat diffusion occurs at very high temperature *without* any reaction. A

Table 2. Comparison of characteristic features of classical SHS and MASHS in case of FeAl synthesis [24, 25]

	Ignition temperature T_{ig}, °C	Combustion temperature T_c, °C	Combustion front velocity U, mm s^{-1}	Heating rate v_h, deg s^{-1}
MA + SHS	400	930	12	1600
SHS	500	900	3	480

simple 1D model, with thermal diffusivity and a heat loss coefficient as only parameters, has then been used to estimate the thermal diffusivity of the material using a dichotomy method based on the gold number, in order to fit the experimental data.

This method has been applied successfully to different types of materials [39, 40], showing thermal instabilities as well as a regular propagation. On one example, the method has even been applied to a sample before the onset of the reaction. For the results to be valid, the complete lack of reaction (or of a secondary reaction) has to be proven. In the present case, the method has been applied to a sample undergoing simultaneously TRXRD, a peak shift corresponding to the temperature variation (and thus the corresponding evolution of the lattice parameter) could be observed; aside from this, the X-ray pattern remains unchanged. As an example, the thermal diffusivity of the sample for which the method was first established was estimated at $(2 \pm 0.2) \times 10^{-6}$ m^2 s^{-1}.

However, because front propagation velocities are the resultant of many parameters, a clear understanding of their influence taken globally is extremely difficult. For example, separating the influence of macroscopic parameters, such as granulometry and initial porosity is an almost impossible task when a model has to be constructed from scratch. With this method however,
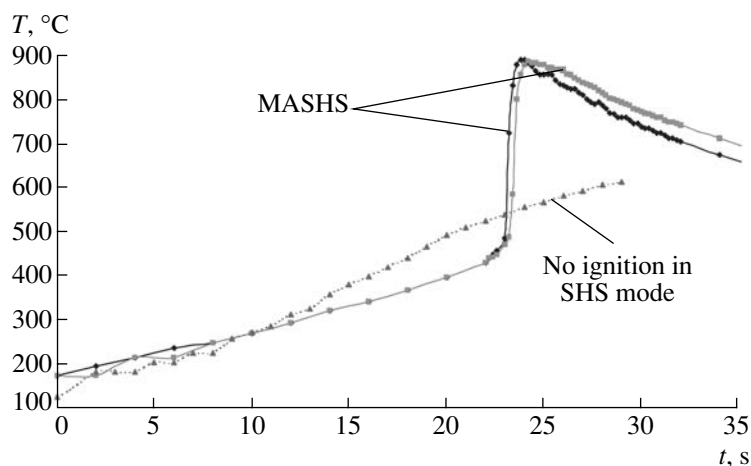

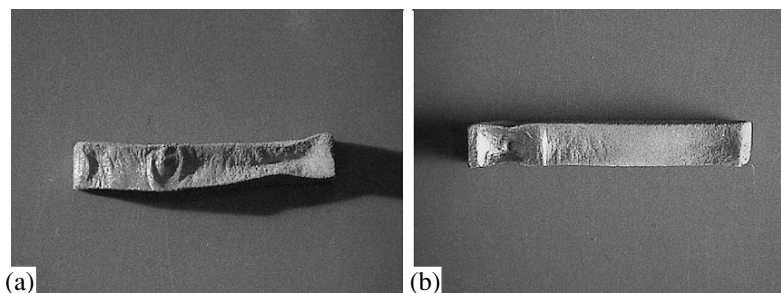**Fig. 9.** MA makes possible the SHS reaction Fe + 2Si $\longrightarrow$ FeSi$_2$ [32, 33].

Fig. 10. TiN samples SHS-produced at two compaction pressures of green bodies: P_{comp} = 50 (a) and 150 (b) MPa [41].
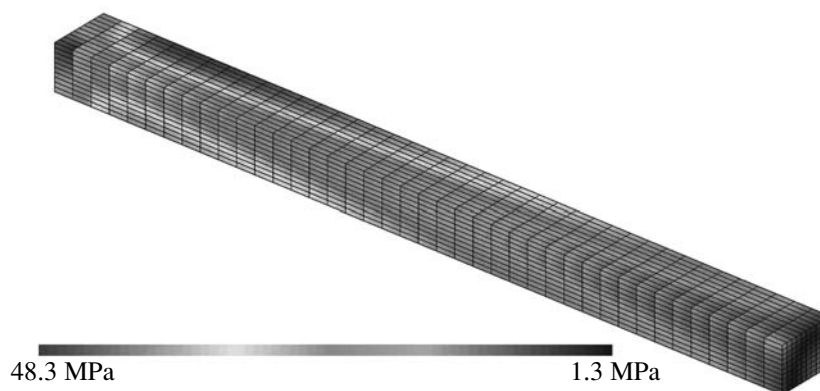

48.3 MPa   1.3 MPa

Fig. 11. Stress field at a nitrogen pressure of 200 MPa and for a supposed isotropic elastic quarter of sample.

because the main influence of initial porosity is on thermal diffusivity, and the main influence of granulometry is on reaction kinetics, the two phenomena could possibly be separated.

MODELING

In order to get, on the one hand, a better understanding of the reaction mechanisms and, on the other hand, a better control of the final microstructure of end products, a great effort has been achieved in the field of modeling. This effort was carried out at the following levels.

Finite Element Simulation

In order to evaluate the consequences of a mechanical strain field on the geometry of a TiN bar synthesized by SHS, undertaken was a finite element computation of the thermo-mechanical behavior of a densified titanium powder bar before the firing temperature. Experimentally, the SHS reaction gives a strongly distorted sample (Fig. 10). These computations refer to the experimental work by Fretty [41] which show that the compaction pressure of the initial powder sample and

the temperature distribution in the furnace have a strong influence on the strain and temperature fields in the sample.

The computed stress field of a quarter of sample when heating in the furnace is stopped at 400° (Fig. 11) shows a strong stress concentration close to the part of the sample where the reaction started. These simulations confirm the existence of correlations between the mechanical strains yielded by experimental conditions and the sample distortions experimentally observed.

Submicron Modeling

Such a modeling was performed for high-temperature synthesis of SiC in order to find parameters controlling the dynamics of formation and microstructure of resultant ceramics. First of all, the following experiments were carried out [42]: heating the sample at a constant rate and holding at a temperature smaller than the eutectic temperature of silicon and carbon; cooling down and determination of the SiC conversion rate by XRD in order to follow the dynamics; and mercury porosimetry in order to determine the size distribution of the pores.

As for the theoretical aspects [43, 44], the model essentially relies on the following hypotheses. A dissolution–precipitation mechanism is assumed with heterogeneous nucleation of SiC at the interfaces between liquid silicon and a solid. The local heat release accompanying the formation of SiC leads to the melting of silicon in the neighborhood of the site where reaction takes place. Temperature remains constant until solid silicon is present. A two-dimensional (2D) cut of the initial mixture is generated as follows: Si disks and C sticks of sizes sampled according to the experimental distributions are generated without overlap in a square box with periodic boundary conditions. The initial number of contacts between C and Si is found to decrease as the radius of Si disks increases. Instead of simulating the movements of liquid silicon and following the evolution of solid silicon sites, the total initial number of solid silicon sites has been determined; so an identical number of potentially liquid silicon sites around the skeleton of carbon sticks were created. To reproduce the formation of SiC, the following simulation procedure was adopted. Calculations start at time t with N_{Rc} reactive sites of silicon Rc in contact with carbon and N_{Rs} reactive sites of liquid silicon Rs in contact with solid Si or SiC, then:

(i) $p_c N_{Rc}$ and $p_s N_{Rs}$ randomly chosen reactive sites transform into SiC sites, where the reaction probabilities obey $p_c < p_s < 1$

(ii) 2 or 3 (in average, 2.65) liquid Si sites form in the neighborhood of each new SiC site according to the ratio of standard enthalpy of reaction and enthalpy of fusion of Si

(iii) the nature (Rc, Rs, or non reactive) of the formed liquid Si sites are determined according to their neighbors and the values of N_{Rc} and N_{Rs} are updated

(iv) time is incremented by Δt

The simulation allows (i) to follow the SiC conversion rate versus time for different mass distributions of the reactants, (ii) to determine the mass distribution of SiC grains when the reaction is complete. The agreement between simulations and experiments is good for both the dynamic and morphological aspects: (a) the smaller the mean size of silicon grains the higher the reaction rate, (b) morphology of the obtained material is such that the mean size of the formed SiC grains is maximal for silicon grains of the same size as the carbon grains (Fig. 12), (c) there is a relation between the size of the SiC grains and the size of the pores. All this allows the control of the porosity down to the submicron scale, and so to prepare silicon carbide filters with high porosity, controlled pore size in the range 1–15 μm, and good mechanical strength.

Mean Field Modeling

The complexity of SHS experiments arises from the coupling between the propagation of a thermal wave and the reactive processes that occur at the level of indi-
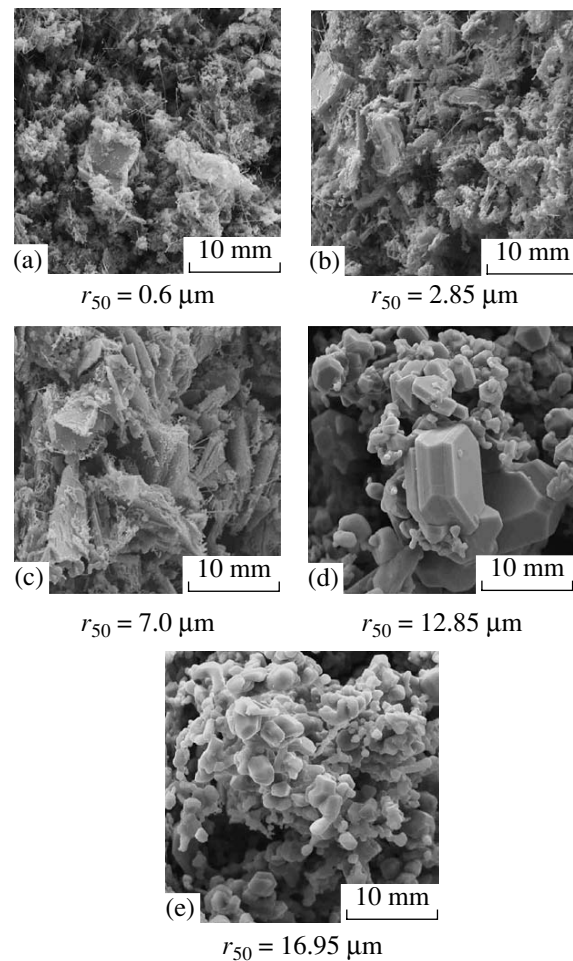

Fig. 12. SEM images of silicon carbide obtained for different medium values r_{50} of silicon grains and the same carbon powder with a medium length $l_{50} = 10.5$ μm. Maximum size of SiC grains is observed for r_{50} between 7 and 12.85 μm.

vidual particles. So, the main objective was to understand the intricate coupling between these phenomena. For that, let us consider reactions in a binary system in which the rise and fall of temperature during the reaction is such that one of the reacting metals melts but not the other. For such a system, using the phase diagram of the binary system, a general theory that describes the reaction taking place in a single solid of one component surrounded by the melt of the second component has been developed [45].

In many situations, the exothermic reaction front propagates in a powder of metallic particles (A and B) whenever one of the reactant (B) melts and surrounds the particles of the other (A). Hence it is essential to model the reaction of a particle A suspended in a molten phase B. In this case, initially A dissolves in B and, as the liquid B diffuses through the solid, layers of intermetallic products can form and propagate inward converting the solid particles of A into the product [46, 47]. At the same time, the outermost surface may
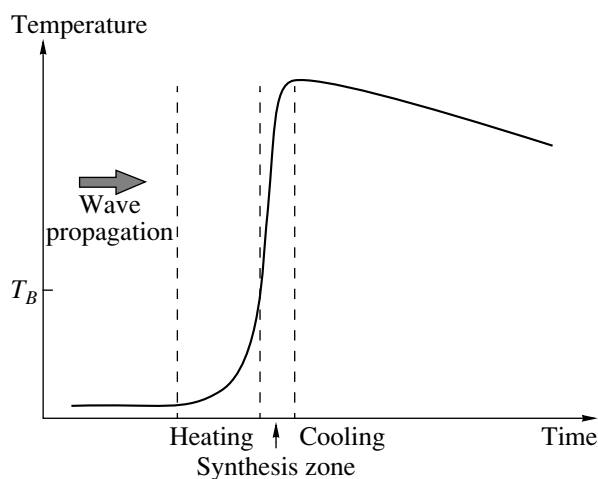
Fig. 13. Typical temperature profile of SHS process. It is the mean temperature variation for each particle in the reacting sample.

slowly dissolve in the melt. For example, in the Al–Ni system [48], Al melts at 933 K and surrounds the Ni particles whose melting point is 1728 K. If the temperature, T, of the reaction does not exceed the melting point of Ni, the formation of the intermetallic compounds is due to liquid–solid reaction. The present model describes such reactions taking into account details and complexity of the reaction based on the phase diagram of the binary system. As the reaction progresses, various intermetallic compounds of the two metals create a multilayer system. Such layered structures have been observed in experiments with metal foils [47] and with powders [46]. The model seeks to describe the growth dynamics of these layers and to predict the final multilayer structure of a typical particle.

In the developed mean field model, considered is a "typical" single solid particle surrounded by a liquid when it experiences a propagating temperature front (Fig. 13).

The reaction proceeds through the following stages (Fig. 14).

(1) First component B melts and surrounds particles of A which are assumed to be spherical for simplicity, but other shapes could also be considered.

(2) Next, particle A begins to dissolve into liquid B and, at the same time, B diffuses into A and forms a layer of intermetallic compound, say α.

(3) Since the A/α interface is not in equilibrium, driven by the diffusion of B (more accurately, interdiffusion of A and B) through the α layer, more of A converts to α. Thus, the thickness of the α layer grows.

(4) At the outer surface of the α layer, B may react with the α phase to produce another intermetallic compound β resulting in the growth of a β layer. Similarly, more layers, γ, δ, etc., could form successively, depending on the number of compounds that the components A and B can form.

(5) The outermost layer dissolves into the melt thus changing composition of the melt.

The theory gives a set of kinetic equations that describe the propagation of the phase interfaces in the solid particle and the composition change of the melt that surrounds it. In our work, we have derived a set of equations for one- and two-layer systems in which each layer is a binary compound in the phase diagram. The system of equations can be solved for different realistic systems, like the Al–Ni system, to illustrate the applicability of the theory.

Using this approach, it is possible to investigate the effect of various parameters—such as the initial grain size, diffusivities, cooling rate or heat of reaction—on development of the global reactive process (for example, see Fig. 15). This model proves to be quite helpful for interpreting the experimental observations and for understanding the microstructural properties of the final material.
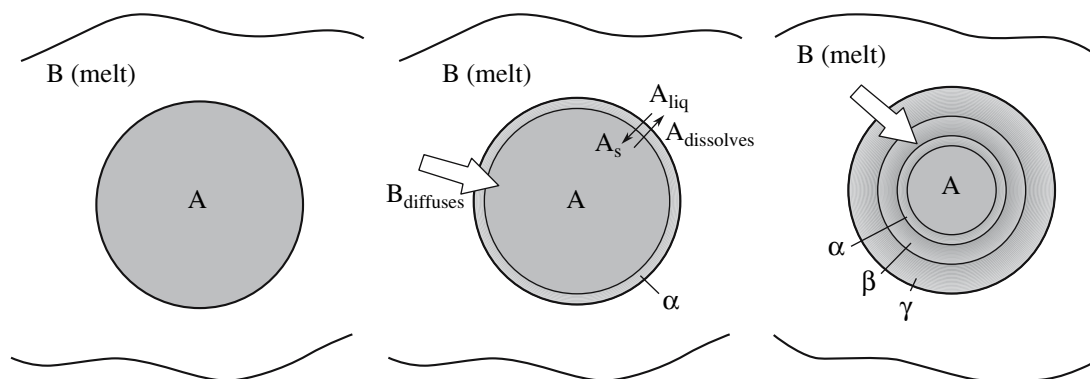

Fig. 14. Different stages of the reaction between two metals, A and B. The highest temperature the system reaches is higher than the melting point of A.
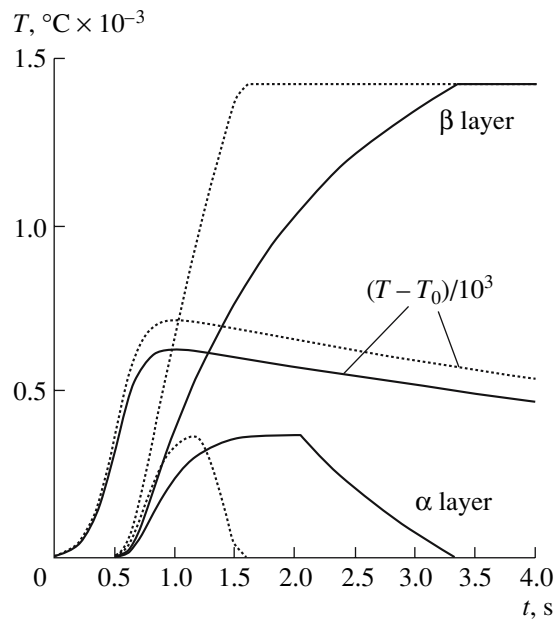
Fig. 15. Evolution of the thickness of the α layer and β layer when the system is subjected to temperature profiles that differ in the maximum value reached. The dotted and solid curves for the α and β layer correspond to the dotted and solid temperature curves, respectively. When the temperature maximum value is lower, we find a significant difference in the evolution of the system. It appears that the maximum temperature has a strong influence in the microstructural properties: the process may be incomplete after the passage of the front when the combustion temperature is not high enough. This particular situation may lead to incomplete conversion of A that is surrounded by the α layer, as may be observed in some experiments or by sample quenching.

SHS AS A FRUITFUL WAY TO APPLICATIONS

Heat Generation

The aim of this research was to study extremely exothermic reactions with the general purpose of using the heat generated. As a general rule, the material studied here could be of secondary importance. Presently, the chosen system for this study was based on the reduction of nickel monoxide with aluminum according to the scheme $3NiO + 2Al \longrightarrow 3Ni + Al_2O_3$. However, the stoichiometry has been varied, so that the final products could be alumina and nickel or alumina and a nickel aluminide. Moreover, in order to follow the reaction, a way to slow down the reaction had to be found. Therefore, a diluent was used; this diluent could be either alumina, zirconia, or even another oxide that could react (as a secondary reaction) with the alumina produced by the main reaction such as magnesia ($MgO + Al_2O_3 \longrightarrow MgAl_2O_4$) or titania ($TiO_2 + Al_2O_3 \longrightarrow TiAl_2O_5$).

Samples were thoroughly mixed, compacted to a green density of about 60%, and then allowed to react in our reaction chamber [1]. Stoichiometry was varied with the goal of producing the following final products
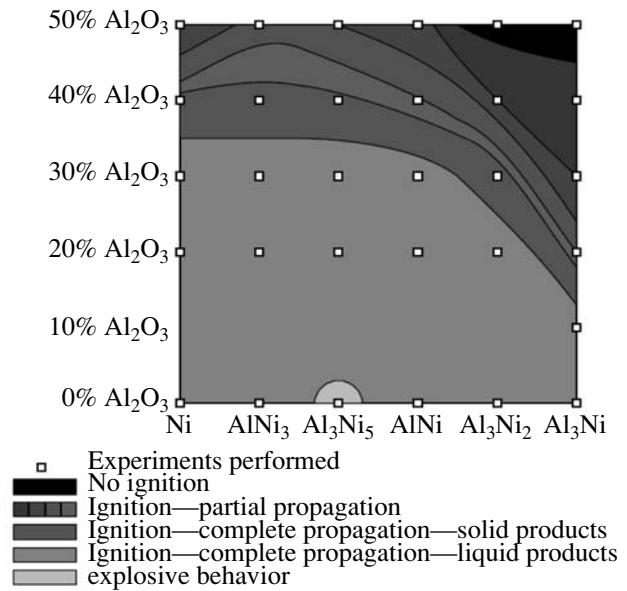

Fig. 16. Experience map showing the reactive behavior as a function of the initial composition (abscissa) and diluent concentration (ordinate).

(aside from alumina): Ni, Ni_3Al, NiAl, Ni_2Al_5, and $NiAl_3$. The above mentioned diluents were used, with a mass percentage calculated so that the heat capacity of the diluent represented 0, 10, 20, 30, 40 or 50% of the overall heat capacity of sample.

Macroscopic behavior of these reactions is illustrated in Fig. 16 [49]. It follows that, with increasing Al content of aluminides, the exothermicity decreases and that low-diluent mixtures yield liquid products within the almost entire range studied. With no diluent, explosive behavior can be observed.

Microscopic behavior has also been studied, and especially the low-scale demixion that can occur due to the molten state of one if not both resulting products [40]. Such a system can be applied in many different ways. The most obvious one is the so-called chemical oven, when the SHS reaction is used with the only purpose of generating heat, which is a realistic use in the present case because of the low cost of the initial products. Through the use of various stoichiometries and various diluents, the versatility of the system has been proved. It could therefore be used co-mixed with a metal–carbon system, as nickel is well known to be a good sintering aid for carbides. Naturally, it could also be used to synthesize complex oxides such as spinel structures.

Similar approach has been applied to the solid–gas mixtures (Zr/ZrO_2) in oxygen in order to monitor in situ the kinetics of solid–gas SHS reactions [50].

SHS of Max Phases

The Ti_3SiC_2 ternary compound is a MAX phase which has received increasing attention because it combines the attributes of both metals and ceramics [51–53]. Like metals, it has good electric and thermal conductivities, a relatively low hardness and a high fracture resistance. Moreover, it is easy to machine using conventional tools. Ti_3SiC_2 is also oxidation-resistant and extremely refractory like ceramics. Those properties make this MAX compound a promising candidate for structural applications at high temperatures (turbine blades, electric contacts, bearings, etc.).

Several methods to prepare the Ti_3SiC_2 phase have been investigated: the MAX phase was first obtained as a thin film by CVD [54], and then as a bulk sample by arc melting [55], by direct sintering [9, 56, 57] or by reactive hot pressing [58, 59]. Nevertheless, none of these methods have produced a single Ti_3SiC_2 phase. In addition to these traditional preparation methods, SHS has also been used to produce Ti_3SiC_2 [6, 12, 60–63]. The SHS of Ti_3SiC_2—both from elemental starting materials (Ti, Si, C) [6, 12, 60–63] and from SiC as a source of silicon [64, 65]—was carried out using the propagation mode [61, 63, 65] or the thermal explosion mode [6, 12, 64, 65]. The Ti_3SiC_2 content never exceeded 60%. The resulting Ti_3SiC_2 product was reported to contain the Ti–C [6, 12, 60–64], Ti–Si [12, 62] binary phases, and occasionally, small amounts of $Ti_5Si_3C_x$ [64].

In the beginning of this paper, we reported on the synthesis of Ti_3SiC_2 by SHS using the propagation mode, starting with titanium, silicon and graphite powders. In order to propose a mechanism for the formation of Ti_3SiC_2, structural and thermal evolutions of the sample have been studied in the moving combustion front. The extreme rapidity of the SHS imposes the use of a synchrotron X-ray beam and a fast detection system to provide detailed information on the reaction pathways and phase transformations during the Ti_3SiC_2 formation. Furthermore, the thermal evolution during the combustion reaction has been determined by IR thermography. However, as stated previously [5], up to now the reaction mechanism is not fully understood. Moreover, a full conversion of the reactants into a pure MAX phase has been never obtained. So, new investigations are still needed in order to get a good control of the SHS of such an interesting ternary phase.

SHS of SiAlON

SiAlONs are used as high temperature engineering materials, for cutting tools and also as abrasive materials. Their SHS under nitrogen pressure has already been investigated. However, the addition of Si_3N_4 or SiAlON in the reactant mixture is needed to ignite the reaction and obtain high conversion rates. Nevertheless, the presence of additives increases the cost of the process. Thus, the aim of this work was to re-investigate the SiAlON formation by SHS without using additives. The challenge was to modify the initial conditions in order to ignite the reaction and to get high conversion rate with a product free from additional phases.

In a previous study, the SHS of Si_3N_4 was ignited at the melting point of silicon [66]. The reaction occurred between liquid silicon and nitrogen gas. If silicon is not isolated from nitrogen, this reaction should also result in the formation of SiAlON. Then, in the raw mixture, reactants need to be intimately mixed to get a high conversion rate and silicon grains need to be isolated from nitrogen to prevent the formation of Si_3N_4.

Two kinds of SiAlON phases were prepared, Si_2N_2O and β-SiAlON [67–69]. The reactant mixtures consisted of silicon plus silica and silicon plus mullite ($2SiO_2$–$3Al_2O_3$), respectively. The mixtures were prepared from a liquid solution to get silicon grains surrounded by silica or mullite. These powders were compacted, placed into a furnace under nitrogen pressure and heated at a high rate (90° deg min^{-1}). The reaction was ignited on one side of the sample and because of the existence of a thermal gradient (the furnace only consists of one heating zone) the direction of propagation was controlled. The temperature profiles were measured by means of three thermocouples and recorded during the reaction. The initial blends and the SHS samples were characterized by XRD and SEM. Rietveld refinements were performed for phase quantification. The XRD patterns and Rietveld refinements show that high conversion rates can be obtained in these experimental conditions for low nitrogen pressures; 97 wt % Si_2N_2O and 79 wt % β-SiAlON were obtained at 2 and 6 MPa, respectively. The SHS products only constituted of SiAlON and unreacted silicon, no additional phase was evidenced. These high conversion rates were ensured by the preparation of starting powders. As follows from SEM images, silicon grains are surrounded by silica (Fig. 17a) or mullite, thus the contact between the solid reactants is very high and the direct access of nitrogen to silicon is prevented (at least at low pressures).

Based on the above results, the following mechanism for formation of the SiAlON phases by SHS was suggested. First, when the temperature of the compact reaches 1416°C the silicon melts. Then the melted silicon dissolves the surrounding silica or mullite and nitrogen can be incorporated into this liquid. Finally, when the liquid composition corresponds to the stoichiometric one, Si_2N_2O or β-SiAlON is formed. The SEM micrograph of β-SiAlON is presented in Fig. 17b. Two phases are observed, Si (light grey) and SiAlON (mid grey). The dark grey regions correspond to holes. The rounded shape of the silicon grains reveals the existence of a transient liquid, which confirms the melting of this phase.
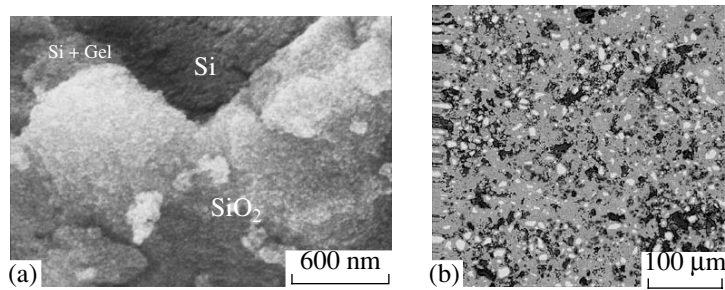
Fig. 17. SEM micrographs of (a) a raw mixture for Si_2N_2O synthesis and (b) p-SiAlON obtained by SHS under 6 MPa of nitrogen.
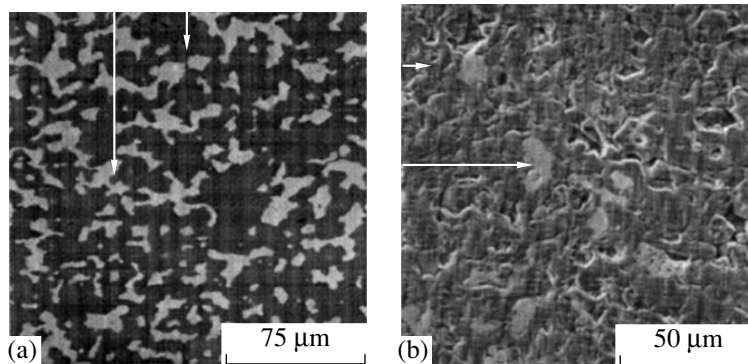

Fig. 18. Microstructure of two dense Al_2O_3–$MoSi_2$ composites: (a) 66.7% Al_2O_3/33.3% $MoSi_2$ (molar) and (b) 54.5% Al_2O_3/45.5% $MoSi_2$ (molar).

Contribution to Mullite Synthesis via SHS

Mullite ceramics exhibit attractive physical properties (low thermal expansion, good thermal stability, creep resistance, etc.) for applications as dense or porous materials. SHS processing of porous mullite bodies from kaolinite clay–aluminum mixtures has been undertaken [70]. Results clearly show that the synthesis of high-porosity products containing mullite can be envisaged by SHS reaction in oxygen atmosphere and addition of Mg and Al powders to preheated kaolinite clays. Porous black colored bodies are obtained. The samples are composed of mullite, corundum, quartz, and silicon. When a hot post-treatment is applied in air, the porosity is maintained while the dark color disappears. The dark color comes from reduction of silica with Al. The porosity of the obtained compacts seems to be controlled by the grain size of metallic powders.

SHS OF COMPOSITES

NiAl–ZrO₂ Composites

The so-called MMC (Metallic Matrix Composites) with a matrix of intermetallic material are high-temperature structural materials, light and corrosion-resistant, that can be used in aircraft turbines. In our case, the reaction is triggered by Al melting, and $NiAl_3$ and Ni_2Al_3 occur transiently before the formation of NiAl [71]. The dense composite can be produced by combining thermal explosion with a post thermal cycle [72]. The microstructure of the composite can be controlled by using a diluent.

Dense MoSi₂–Al₂O₃ Composites

These materials exhibit elevated resistance to oxidation at low temperatures and to creep at high temperatures (possibility for preparation of $MoSi_2$-based resistors for high-temperature applications): Such composites with different alumina contents have been prepared using the SHS reaction between molybdenum trioxide, aluminum and silicon or silica at room temperature [73–75]. A comprehensive study of the relation between $MoSi_2$ or Al_2O_3 dilution, microstructure, and the maximum temperature achieved during the SHS reaction have lead to the preparation of dense composites (relative density higher than 92%) with a molar molybdenum disilicide content in the range 17–74% and homogeneous phase distribution (Fig. 18). The densification results from the application of a weak
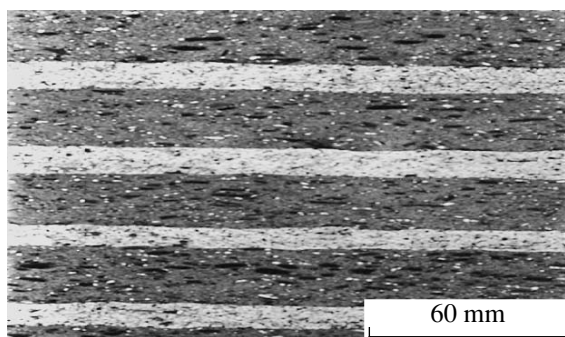
Fig. 19. FMG material comprising alternating Al_2O_3–$MoSi_2$-rich layers.

load after the end of heat propagation in the SHS step. Characterization of these materials has shown that the presence of alumina has a very positive influence on the resistance of $MoSi_2$-based material against low-temperature oxidation and high-temperature creep.

$MoSi_2$–Al_2O_3-Based FGM

These materials have been prepared by combining tape casting, SHS, and forging [76–78]. Tapes of MoO_3, SiO_2, and Al mixtures corresponding to different $MoSi_2/Al_2O_3$ ratio have been prepared, stacked, thermally pressed, bound?, and densified by forging (Fig. 19). Depending on the evolution of the composition of successive layers of the stack, different gradients in electric properties, in creep behavior or in corrosion resistance have been obtained.

Joining of Alumina-Based Refractories

The conditions for joining of alumina-based refractory materials by using the SHS reaction between Al, SiO_2, and $MoSi_3$ have been explored. Very efficient joining has been obtained by igniting a thermal explosion at 700°C in a reactive layer comprising of a sto-

ichiometric mixture of starting components placed between the refractory parts. The quality of the joining (Fig. 20) strongly depends on the residual porosity present in the refractory parts since this porosity tends to coalesce at the boundary of the melting zone.

Repairing and Coating

Hard coatings, such as carbide coatings, are usually used for increasing the surface hardness of ceramics or metals. Due to the very high liquidus temperature of carbides, gas-tight coatings are very difficult to obtain by thermal spraying. An SHS reaction has been used in order to introduce the additional energy necessary to obtain complete melting [79, 80]. Plasma spraying of granules containing a mixture of graphite and titanium has been performed in air. The influence of granule stability, during the flight in the plasma, on the resulting coating composition and morphology has been studied. When the SHS reaction occurs during the flight, TiC-based coating with an irregular morphology is obtained. When the contact between C and Ti is not maintained in the plasma (unstable granules), a new compound $Ti_{0.81}C_{0.05}$ is formed on the support. Pure and dense coatings of this new compound, with a high value of hardness (Vickers hardness 1000 HVz) have been obtained (Fig. 21).

Simultaneous Repairing and Coating of Ni-Based Superalloys

This technique is designed to simultaneously repair and coat Ni-based superalloys for turbine blades applications. A few years ago, an "SHS build-up" process under pressure was developed for repairing damaged turbine blades. The advantages of this process are the rapidity, self-generation of energy and, because of a local treatment of the turbine component, the increase in the allowed number of repairs. The aim of this work is to show that this process can be extended to simultaneous repairing and coating.
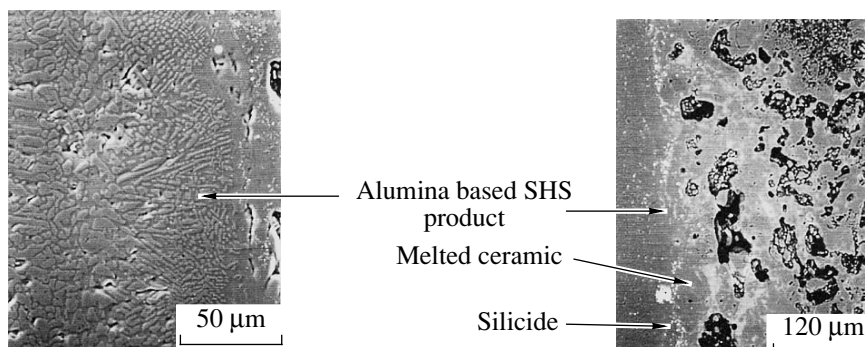

Fig. 20. Example of joining between the alumina and cordierite refractory parts.
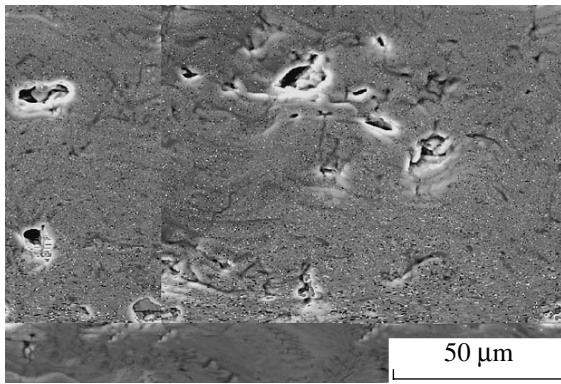
Fig. 21. Cross section of the $Ti_{0.81}C_{0.05}$ coating deposited by combining SHS reaction and thermal spraying.
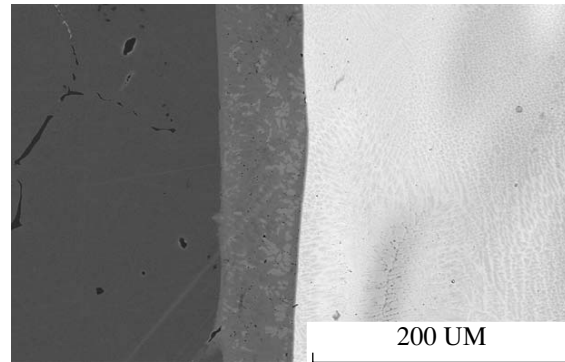

Fig. 22. SEM micrograph of (Ni, Pt)Al with 12 at % Pt: P_{comp} = 100 MPa, v_{heat} = 50 deg min^{-1}, m = 0.5 g.

In the "SHS build-up" process, a brazing foil is inserted between a Ni-based superalloy substrate and a reactant compact made of the 50 at % Ni–50 at % Al mixture. The joining system is located in a boron nitride crucible. The crucible is inserted into a furnace with one heating zone where the temperature is measured by means of three thermocouples and recorded during the reaction. Finally, the furnace is placed in a high-pressure device with argon used as a pressure medium. By heating the sample at high speed, the combustion synthesis of NiAl is ignited in the compact and the heat released during this reaction gives rise to interdiffusion of the elements and consequently to joining. To perform simultaneous repairing and coating of the Ni-based superalloy, platinum is added to the reactant compact. Pt-modified NiAl coatings are well known to show a very high resistance to high-temperature corrosion [81].

The influence of Pt content on the combustion synthesis of NiAl was studied upon variation in process parameters. The values previously optimized for the SHS build-up process [82, 83] were taken as the starting point of this study. They were as follows: P_{Ar} = 50 MPa, v_h = 90 deg min^{-1}, G_{Ni} = 10 µm, G_{Al} = 30 µm, P_{comp} = 50 MPa, m = 1 g. Nevertheless, because of platinum addition, alternative values were tested for v_h = 50 deg min^{-1}, P_{comp} = 100 MPa, and the compact weight m = 0.5 and 0.7 g. The average grain size of Pt was G_{Pt} = 2 µm, and the tested values for platinum content were 5, 8, 12, and 18 at %. The maximum value was chosen to be the highest solubility of platinum in NiAl at 1000°C [84], which is the working temperature for turbine blades. Indeed, the presence of precipitates at this temperature is harmful for the coating ductility [85].
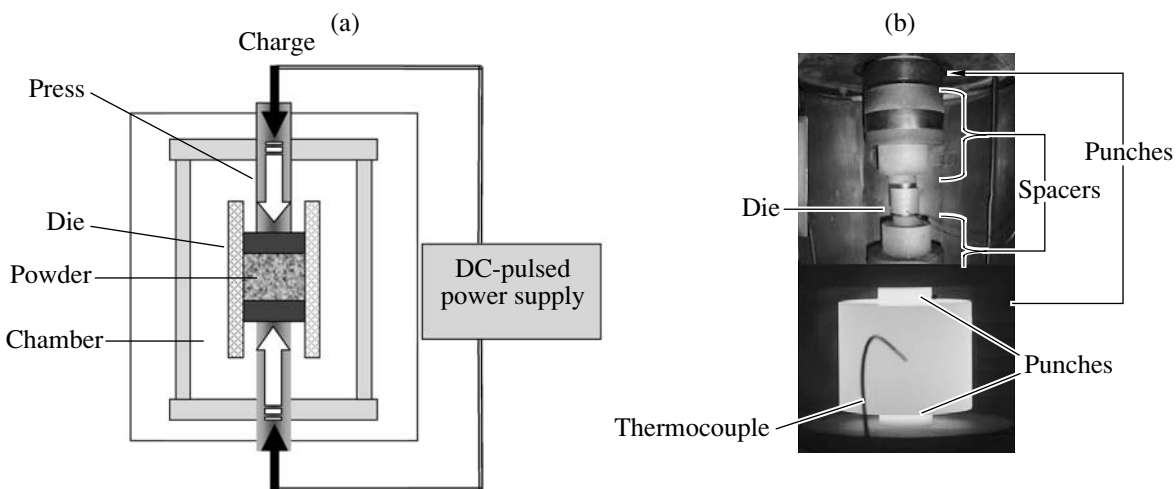

Fig. 23. (a) General sketch of an SPS machine and (b) overall view of the mould environment (above) and of the hot mould during experiment (below).

Table 3. Comparative analysis of the SPS and FAPAS technologies for some systems whatever the type of sintering (reactive or not)

System	Process	Phases	Density*	Crystallite size*
Fe–Al	FAPAS	FeAl	96–99%	50–120 nm
(1750 A, 70 MPa, 4 min)	SPS	FeAl	96–99%	50–120 nm
Mo–2Si	FAPAS	$MoSi_2$	90–93%	60–100 nm
(1500 A, 100 MPa, 5 min)	SPS	$MoSi_2$	91–94%	70–110 nm
0.6Fe–0.4Al	FAPAS	$Fe_{0.6}Al_{0.4}$	97–99%	100–150 nm
(1750 A, 80 MPa, 7 min)	SPS	$Fe_{0.6}Al_{0.4}$	97–99%	90–120 nm
α-Fe_2O_3 (sintering)	FAPAS	α-Fe_2O_3	95%	350 nm
(1750 A, 50 MPa, 5 min)	SPS	α-Fe_2O_3	98%	>1 µm
Al_2O_3 (sintering)	FAPAS	Al_2O_3	97–99%	>1 µm
(1750 A, 50 MPa, 7 min)	SPS	Al_2O_3	95–99%	>1 µm

* Density and crystallite size are independent.

Because high temperatures and high speeds of reaction are usually reached during combustion synthesis, materials obtained by SHS are very porous. Nevertheless, the porosity of the coating was found to decrease with decreasing v_h and increasing Pt content.

In contrast, the combustion temperature and the exothermicity of the reaction increase with Pt content. This heat which is transferred to the substrate could lead to higher damages in the superalloy. Indeed, the formation of dendrites was observed by SEM in the substrate of the sample with 12 at % Pt. In order to avoid these damages, some parameters, such as P_{comp} and m, were modified. At elevated P_{comp}, dissipation

Fig. 24. Growth kinetics for $MoSi_2$ during oxidation in air at 673 K [89]: (◆) dense microstructured $MoSi_2$, coherently diffracting domain size >250 nm, density 93–97% and (■) dense nano-organized $MoSi_2$, coherently diffracting domain size 50–100 nm, density 92–94%.

becomes higher but nevertheless the dendrites are still present. In contrast, when m was reduced, the dendrites disappeared (Fig. 22). Similar results were obtained for the samples with a platinum content of 18 at %.

The optimized parameters for simultaneous repairing and coating of Ni-based superalloys with our equipment were found to be as follows: $P_{Ar} = 100$ MPa, $v_h = 50$ deg min^{-1}, $P_{comp} = 50$ MPa, and $m = 0.5$ g.

Two samples prepared in the optimized conditions, one with 18 at % Pt and another without Pt, were treated under air at 1050°C for approximately 100 h. In both cases, an oxide layer which is indicative of passivation was evidenced. Nevertheless, this oxide layer showed a better adhesion to the coating for the Pt-containing sample. Therefore, the protective function of the platinum aluminide coatings synthesized by SHS has been successfully realized [86].

PRODUCTION OF FULLY DENSE NANO-INTERMETALLICS BY REACTIVE SHS SINTERING IN AN SPS MACHINE

A few years ago, the simultaneous effect of an electrical field combined with an applied pressure during the combustion, using the so-called Field-Activated Pressure-Assisted Synthesis (FAPAS), was found to be suitable to produce good quality dense intermetallic compounds in a *one-step process*. Consequently, the application of this technique to mechanically activated powder mixture gave birth to a new SHS process (MAFAPAS) [87].

The applicability of this new approach to the simultaneous synthesis and densification of nanomaterials has been demonstrated for the Fe–Al, Nb–Al, and Mo–2Si systems. Mechanically activated reactant powders were placed inside a graphite die and subjected to
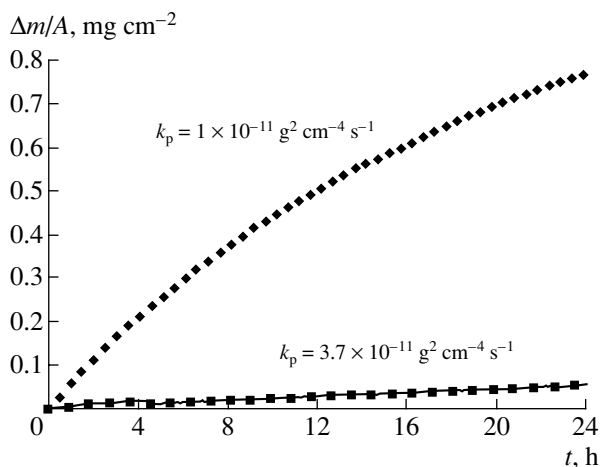
uniaxial pressing, and a heavy pulsed electric current was passed through the die (Fig. 23). After reactive sintering (for 2–5 min), the samples acquired a relative density above 95%. The nanostructured products comprised of the desired phases with little or no amount of secondary phases. For example, this process was successfully applied to produce nanocrystalline (32–89 nm) bulk FeAl intermetallic compacts with a relative density close to 99%. In addition, other dense nanostructured materials, such as $MoSi_2$ or $NbAl_3$, have been elaborated suggesting that this technique can provide an alternative route to the formation of dense nanomaterials in which the consolidation and synthesis steps are accomplished simultaneously. For the same purpose (MASPS), classical SPS machines have also been successfully used (Table 3) [88]. In addition, nanostructured and fully dense $MoSi_2$ exhibited [89] a high resistance to dry corrosion in air (Fig. 24).

CONCLUSIONS

Both in situ TRXRD and IR thermography, on the one hand, and different levels of modeling, on the other, have generated a strong progress in the knowledge and the control of many SHS reactions. The SHS of simple binary materials, such as intermetallics (FeAl, $MoSi_2$, $NbAl_3$, etc.), oxides (e.g. ZrO_2), carbides (e.g. SiC) or nitrides, more complex materials, such as mullite, SiAlONs, MAX phases, composites (SiO_2–Al_2O_3, NiAl–ZrO_2), powders in their more complicated states, such as well controlled microstructures, fully densified intermetallics, smart composites, hard coatings carried out by GFA researchers greatly contributed to the worldwide competition to harness the potential of SHS.

ACKNOWLEDGMENTS

REFERENCES

1. Vrel, D., Girodon-Boulandet, N., Paris, S., Mazue, J.F., Couqueberg, E., Gailhanou, M., Thiaudiere, D., Gaffet, E., and Bernard, F., *Rev. Sci. Instr.*, 2002, vol. 73, no. 2, p. 422.

2. Paris, S., Gaffet, E., Vrel, D., Thiaudiere, D., Gailhanou, M., and Bernard, F., *Sci. Sinter.*, 2005, vol. 37, p. 27.

3. Cabouro, G., Chevalier, S., Gaffet, E., Vrel, D., Boudet, N., and Bernard, F., *Acta Mater.*, 2007 (in press).

4. Bernard, F., Paris, S., Vrel, D., Gailhanou, M., and Gaffet, E., in *SHS: Concepts of Current Research and Development*, Merzhanov, A.G., Ed., Chernogolovka: Territoriya, 2003, pp. 17–29.

5. Gauthier, V., Cochepin, B., Vrel, D., and Dubois, S., *J. Am. Ceram. Soc.*, 2006, vol. 89, no. 9, p. 2899.

6. Pampuch, R., Raczka, M., and Lis, J., *Int. J. Mater. Prod. Technol.*, 1995, vol. 10, nos. 3–6, pp. 316–324.

7. Huang, T.Y. and Chen, C.C., *Mater. Sci. Forum*, 2005, vols. 475–479, pp. 1609–1614.

8. Grigoryan, H.E., Rogachev, A.S., Ponomarev, V.I., and Levashov, E.A., *Int. J. SHS*, 1998, vol. 7, no. 4, pp. 507–516.

9. Wu, E., Kisi, E.H., and Riley, D.P., *J. Am. Ceram. Soc.*, vol. 85, no. 12, pp. 3084–3086.

10. Riley, D.P., Kisi, E.H., Wu, E., and McCallum, A., *J. Mater. Sci. Lett.*, 2003, vol. 22, pp. 1101–1104.

11. Zhang, Y., Zhou, Y.C., and Li, Y.Y., *Scr. Mater.*, 2003, vol. 49, pp. 249–253.

12. Khoptiar, Y. and Gotman, I., *J. Eur. Ceram. Soc.*, 2003, vol. 23, pp. 47–53.

13. Lis, J., Pampuch, R., and Stobierski, L., *Int. J. SHS*, 1992, vol. 1, p. 401.

14. Yu, R., Zhan, Q., He, L.L., Zhou, Y.C., and Ye, Y.Q., *Acta Mater.*, 2002, vol. 50, pp. 4127–4135.

15. Suryanarayana, C., *Prog. Mater. Sci.*, 2001, vol. 46, p. 1.

16. Gaffet, E., Bernard, F., Niepce, J.-C., Charlot, F., Gras, C., Le Caer, G., Guichard, J.L., Delacroix, P., Mocellin, A., and Tillement, O., *J. Mater. Chem.*, 1999, vol. 9, p. 305.

17. Zeghmati, M., Duverger, E., and Gaffet, E., *Proc. 15th Congr. Canad. Mechan. Appl. (CANCAM'95)*, Tabarrock, B., and Dost, S., Eds., 1995, vol. 2, p. 952.

18. Charlot, F., Gaffet, E., Zeghmati, B., Bernard, F., and Niepce, J.-C., *Mater. Sci. Eng. A*, 1999, vol. 262, p. 279.

19. Gauthier, V., Josse, C., Bernard, F., Gaffet, E., and Larpin, J.-P., *Mater. Sci. Eng. A*, (1999), vol. 265 p. 117.

20. Gras, Ch., Vrel, D., Gaffet, E., and Bernard, F., *J. Alloys Comp.*, 2001, vol. 314, nos. 1–2, p. 240.

21. Bernard, F., Paris, S., and Gaffet, E., *Adv. Sci. Technol.*, 2006, vol. 45, pp. 979–988.

22. Bernard, F. and Gaffet, E., *Int. J. SHS*, 2001, vol. 10, no. 2, p. 109.

23. Gras, Ch., Bernard, F., and Gaffet, E., *Intermetallics*, 2006, vol. 14, no. 5, p. 521.

24. Charlot, F., Bernard, F., Gaffet, E., Klein, D., and Niepce, J.-C., *Acta Mater.*, 1999, vol. 47, no. 2, pp. 619–629.

25. Charlot, F., Gaffet, E., Zeghmati, B., Bernard, F., and Niepce, J.-C., *Mater. Sci. Eng. A*, 1999, vol. 262, pp. 279–288.

26. Gras, Ch., Charlot, F., Gaffet, E., Bernard, F., and Niepce, J.-C., *Acta Mater.*, 1999, vol. 47, no. 7, p. 2113.

27. Moore, J.J., and Feng, H.J., *Prog. Mater. Sci.*, 1995, vol. 39, p. 243.

28. Moore, J.J. and Feng, H.J., *Prog. Mater. Sci.*, 1995, vol. 39, p. 272.

29. Deevi, S.C. and Thadhani, N.N., *Mater. Sci. Eng. A*, 1995, vol. 192, p. 204.

30. Song, T.H., Lee, H.L., Pai, C.H., and Mitsuhashi, T., *J. Mater. Sci. Lett.*, 1995, vol. 14, p. 1715.

31. Munir, Z.A., *Ceram. Bull.*, 1988, vol. 2, p. 342.

32. Gras, Ch., Gaffet, E., Bernard, F., and Niepce, J.-C., *Mater. Sci. Eng. A*, 1999, vol. 264, p. 94.

33. Gras, Ch., Berstein, N., Gaffet, E., and Bernard, F., *Intermetallics*, 2002, vol. 10, p. 271.

34. Bernard, F., Souha, H., and Gaffet, E., *Mater. Sci. Eng. A*, 2000, vol. 284, p. 301.

35. Gras, Ch., Zink, N., Bernard, F., and Gaffet, E., Assisted Self-Sustaining Combustion Reaction in the Fe–Si System: Mechanical and Chemical Activation, *Mater. Sci. Eng. A*, 2007, vol. 456, pp. 270–277.

36. Lagerbom, J., Tiainen, T., Lehtonen, M., and Lintula, P., *J. Mater. Sci.*, 1999, vol. 34, p. 1477.

37. Zhang, Y. and Stangle, G.C., *J. Mater. Res.*, 1995, vol. 10, no. 4, p. 1992.

38. Gras, Ch., Bernard, F., and Gaffet, E., *Intermetallics*, 2006, vol. 14, no. 5, p. 521.

39. Vrel, D., Karnatak, N., Beaufort, M.F., and Dubois, S., *Eur. Phys. J. B*, 2003, vol. 33, pp. 31–39.

40. Vrel, D., Karnatak, N., Heian, E.M., Dubois, S., and Beaufort, M.F., *Int. J. SHS*, 2004, vol. 12, no. 4, pp. 249–259.

41. Carole, D., Frety, N., Etienne-Calas, S., Merlet, C., and Marin-Ayral, R.-M., *Mater. Sci. Eng. A*, 2006, vol. 419, nos. 1–2, pp. 365–371.

42. Morancais, A., Louvet, F., Smith, D.S., and Bonnet, J.-P., *J. Eur. Ceram. Soc.*, 2003, vol. 23, p. 1949.

43. Lemarchand, A. and Bonnet, J.-P., *J. Eur. Ceram. Soc.*, 2006, vol. 26, p. 2389.

44. Lemarchand, A. and Bonnet, J.-P., *J. Phys. Chem. C*, 2007, vol. 111, p. 10829.

45. Baras, F. and Kondepudi, D., *J. Phys. Chem. B*, 2007, vol. 111, p. 6457.

46. Biswas, A. and Roy, S.K., *Acta Mater.*, 2004, vol. 52, p. 257.

47. Zhu, P., Li, J.C.M., and Liu, C.T., *Mater. Sci. Eng. A*, 1997, vol. 239, p. 532.

48. Varma, A., Kachelmyer, C.R., and Rogachev, A.S., *Int. J. SHS*, 1996, vol. 5, p. 1.

49. Vrel, D., Hendaoui, A., Langlois, P., Dubois, S., Gauthier, V., and Cochepin, B., *Int. J. SHS,* 2007, vol. 16, no. 2, pp. 62–69.

50. Tingaud, D. and Nardou, F., *Int. J. SHS*, 2007, vol. 16, no. 3, pp. 110–118.

51. Barsoum, M.W. and El-Raghy, T., *J. Am. Ceram. Soc.*, 1996, vol. 79, pp. 1953–1956.

52. El-Raghy, T., Zavaliangos, A., Barsoum, M.W., and Kalidinidi, S., *J. Am. Ceram. Soc.*, 1997, vol. 80, no. 2, pp. 513–516.

53. Barsoum, M.W., El-Raghy, T., and Ogbuji, L., *J. Electrochem. Soc.,* 1997, vol. 144, pp. 2508–2516.

54. Goto, T. and Harai, T., *Mater. Res. Bull.*, 1987, vol. 22, no. 9, pp. 1195–1201.

55. Arunajatesana, S. and Carim, A.H., *J. Am. Ceram. Soc.*, 1995, vol. 78, pp. 663–672.

56. Racault, C., Langlais, F., and Naslain, R., *J. Mater. Sci.*, 1994, vol. 29, no. 13, pp. 3384–3392.

57. Sato, F., Li, J.F., and Watanabe, R., *Mater. Trans.,* 2000, vol. 41, no. 5, pp. 605–608.

58. Li, S.B., Xie, J.X., Zhang, L.T., and Cheng, L.F., *Mater. Sci. Technol.*, 2003, vol. 19, pp. 1442–1446.

59. Tang, K., Wang, C., Huang, Y., Zan, Q., and Xu, X., *Mater. Sci. Eng. A*, 2002, vol. 328, pp. 206–212.

60. Pampuch, R., Lis, J., Stobierski, L., and Tymkiewicz, M., *J. Eur. Ceram. Soc.*, 1989, vol. 5, pp. 283–287.

61. Lis, J., Miyamoto, Y., Pampuch, R., and Tanihata, K., *Mater. Lett.*, 1995, vol. 22, nos. 3–4, pp. 163–168.

62. Lis, J., Pampuch, R., Rudnik, T., and Wegrzyn, Z., *Solid State Ionics,* 1997, vols. 101–103, pp. 59–64.

63. Feng, A., Orling, T., and Munir, Z.A., *J. Mater. Res.*, 1999, vol. 14, no. 3, pp. 925–939.

64. Riley, D.P., Kisi, E.H., Wu, E., and McCallum, A., *J. Mater. Sci. Lett.,* 2003, vol. 22, pp. 1101–1104.

65. Riley, D.P., Kisi, E.H., Hansen, T.C., and Hewat, A.W., *J. Am. Ceram. Soc.*, 2002, vol. 85, no. 10, pp. 2417–2424.

66. Pradeilles, N., Record, M.-C., and Marin-Ayral, R.-M., *Int. J. SHS*, 2006, vol. 15, no. 2, pp. 157–167.

67. Pradeilles, N., Record, M.-C., and Marin-Ayral, R.-M., *J. Eur. Ceram. Soc.*, 2006, vol. 26, no. 13, pp. 2489–2495.

68. Pradeilles, N., Record, M.-C., Marin-Ayral, R.-M., Linde, A.V., Studenikin, I.A., and Grachev, V.V., *Mater. Res. Bull.,* 2007; doi: 10.1016/j.materresbull.2007.02.032.

69. Pradeilles, N., Record, M.-C., Granier, D., and Marin-Ayral, R.-M., *Ceram. Int.*, 2007; doi: 10.1016/j.ceramint.2007.02.017.

70. Esharghawi, A., Penot, C., and Nardou, F., *J. Eur. Ceram. Soc.*, submitted for publication.

71. Tingaud, D., Stuppfler, L., Paris, S., Vrel, D., Bernard, F., Penot, C., and Nardou, F., *Int. J. SHS*, 2007, vol. 16, no. 1, pp. 12–17.

72. Plazanet, L. and Nardou, F., *Int. J. SHS*, 1998, vol. 7, no. 2, pp. 281–292.

73. Dumont, A.L., Smith, D.S., Gault, C., and Bonnet, J.-P., *Int. J. SHS*, 1998, vol. 7, no. 2, pp. 269–279.

74. Dumont, A.L., Smith, D.S., Gault, C., and Bonnet, J.-P., *Ann. Chim., Sci. Mat.*, 1998, vol. 23, no. 1, pp. 11–18.

75. Dumont, A.L., Bonnet, J.-P., and Gault, C. *Proc. ICCM-12,* Instaprint S.A., Paris, 1999, CD ROM ISBN 2-9514526-2-4, paper 568.

76. Bonnet, J.-P., Desiles, S., Dumont, A.L., Chartier, T., Smith, D.S., and Gault, C., *Int. J. SHS*, 1999, vol. 8, pp. 331–338.

77. Dumont, A.L., Bonnet, J.-P., Chartier, T., and Ferreira, J.M.F., *J. Eur. Ceram. Soc.*, 2001, vol. 21, pp. 2353–2360.

78. Desiles, S., Dumont, A.L., Chartier, T., Smith, D.S., Gault, C., and Bonnet, J.-P., *Brit. Ceram. Proc.*, 1999, vol. 60, pp. 569–570.

79. Haller, B., Grimaud, A., Labbe, J.C., and Bonnet, J.-P., *J. Mater. Res.*, 2006, vol. 21, pp. 1770–1774.

80. Haller, B., Bonnet, J.-P., Fauchais, P., Grimaud, A., and Labbe, J.C., *Proc. Int. Thermal Spray Conf. (ITSC 2004)*, Osaka, 2004, CD ROM, 4 pp.

81. Fisher, G., Datta, P.K., Burnell-Gray, J.S., Chan, W.Y., and Soares, J.C., *Surf. Coat. Technol.*, 1998, vol. 110, pp. 24–30.

82. Pascal, C., Marin-Ayral, R.-M., Tedenac, J.C., and Merlet, C., *J. Mater. Proces. Technol.*, 2003, vol. 135, pp. 91–100.

83. Record, M.-C., Pascal, C., Frety, N., Tedenac, J.C., and Marin-Ayral, R.-M., *Int. J. SHS*, 2004, vol. 12, no. 4, pp. 303–312.

84. Jackson, M.R. and Rairden, J.R., *Metall. Trans. A*, 1977, vol. 8, pp. 1697–1707.

85. Moretto, P., Bressers, J., and Arrell, D.J., *Mater. Sci. Eng. A*, 1999, vol. 272, pp. 310–320.

86. De Jouvancourt, H., Record, M.-C., and Marin-Ayral, R.-M., *Mater. Sci. Technol.*, 2007, vol. 23, no. 5, pp. 593–599.

87. Munir, Z.A., Gaffet, E., Charlot, F., and Bernard, F., US Patent 6 200 515, 2001.

88. Bernard, F., Gaffet, E., and Munir, Z.A., *Ceram. Trans.*, 2006, vol. 194, pp. 235–249.

89. Cabouro, G., Chevalier, S., Gaffet, E., Grin, Y., and Bernard, F., *J. Alloys Comp.*, 2007 (in press).